





Article

Effects of Difluorophenyl Substituents on Structural, Redox, and Magnetic Properties of Blatter Radicals

Dmitry Gulyaev¹, Andrey Serykh^{1,2}, Evgeny Tretyakov^{1,*}, Anna Akyeva¹, Mikhail Syroeshkin¹, Dmitry E. Gorbunov³, Svetlana V. Maltseva^{3,4}, Nina P. Gritsan^{3,*}, Galina Romanenko⁵ and Artem Bogomyakov⁵

¹ N. D. Zelinsky Institute of Organic Chemistry, Russian Academy of Sciences, Leninsky Ave. 47, Moscow 119991, Russia; refihis@ioc.ac.ru (D.G.); andreyser200@mail.ru (A.S.); anna.kozmenkova@gmail.com (A.A.); syroeshkin@ioc.ac.ru (M.S.)

² D. Mendeleev University of Chemical Technology of Russia, Miusskaya Pl. 9, Moscow 125047, Russia

³ V. V. Voevodsky Institute of Chemical Kinetics and Combustion, Siberian Branch of Russian Academy of Sciences, Institutskaya Str. 3, Novosibirsk 630090, Russia; dmitry.e.gorbunov@gmail.com (D.E.G.); lana.maltseva04@gmail.com (S.V.M.)

⁴ Department of Physics, Novosibirsk State University, Pirogova Street, 1, Novosibirsk 630090, Russia

⁵ International Tomography Center, Siberian Branch of Russian Academy of Sciences, Institutskaya Str. 3a, Novosibirsk 630090, Russia; romanenko@tomo.nsc.ru (G.R.); bus@tomo.nsc.ru (A.B.)

* Correspondence: tretyakov@ioc.ac.ru (E.T.); gritsan@kinetics.nsc.ru (N.P.G.)

Abstract: Blatter radicals 1-(3,4-difluorophenyl)-(1a) and 1-(2,4-difluorophenyl)-3-phenyl-1,4-dihydrobenzo[e][1,2,4]triazin-4-yl (1b) were prepared in good yields through oxidation of the corresponding amidrazones using MnO₂ in dry CH₂Cl₂. Cyclic voltammetry showed that both radicals are oxidized and reduced chemically and electrochemically reversibly in accordance with –1/0 and 0/+1 processes. EPR spectroscopy indicated that spin density is mainly delocalized on the triazinyl moiety of the heterocycle. The structure of all paramagnets was unambiguously confirmed by single-crystal X-ray diffraction, and two different 1D chains of alternating radicals were identified. 3,4-difluorophenyl-derivatives 1a are packed into columns composed of two kinds of alternating centrosymmetric dimers, having comparatively short intermolecular distances. In crystals of 2,4-difluorophenyl-derivative 1b, the parallel arrangement of bicyclic moieties and phenyl rings favors the formation of 1D regular chains wherein the radicals are related by translation parallel to the crystallographic stacking axis. Magnetic susceptibility measurements in the 2–300 K region showed that in crystals of the radicals, strong antiferromagnetic interactions are dominant. Subsequent fitting of the dependence of χT on T with 12-membered looped stacks gave the following best-fit parameters: for 1a, $g = 2.01 \pm 0.05$, $J_1/k_B = -292 \pm 10$ K (according to BS-DFT calculations $J_2 = 0.12 \times J_1$ and $J_3 = 0.61 \times J_1$); for 1b, $g = 2.04 \pm 0.01$, $J_1/k_B = -222 \pm 17$ K. For comparison, in a nonfluorinated related radical, there are only very weak intermolecular interactions along the columns ($J/k_B = -2.2 \pm 0.2$ K). These results illustrate the magnitude of the influence of the difluorophenyl substituents introduced into Blatter radicals on their structure and magnetic properties.

Keywords: Blatter radicals; fluorinated organic compounds; electrochemically reversible processes; antiferromagnetically coupled chains; magneto-structural correlations



Citation: Gulyaev, D.; Serykh, A.; Tretyakov, E.; Akyeva, A.; Syroeshkin, M.; Gorbunov, D.E.; Maltseva, S.V.; Gritsan, N.P.; Romanenko, G.; Bogomyakov, A. Effects of Difluorophenyl Substituents on Structural, Redox, and Magnetic Properties of Blatter Radicals. *Catalysts* **2023**, *13*, 1206. <https://doi.org/10.3390/catal13081206>

Academic Editor: Kotohiro Nomura

Received: 29 July 2023

Revised: 8 August 2023

Accepted: 10 August 2023

Published: 12 August 2023



Copyright: © 2023 by the authors. Licensee MDPI, Basel, Switzerland. This article is an open access article distributed under the terms and conditions of the Creative Commons Attribution (CC BY) license (<https://creativecommons.org/licenses/by/4.0/>).

1. Introduction

1,3-diphenyl-1,4-dihydrobenzo[e][1,2,4]triazin-4-yl, also known as the Blatter radical [1], was first prepared in 1968 and did not receive much attention [2,3] until the end of the last century when F. Wudl et al. showed that a benzotriazinyl radical forms a pressure-sensitive semiconductor with tetracyanoquinodimethane [4] and Neugebauer et al. reported another paramagnetic derivative with short-range antiferromagnetic ordering [5,6]. Since the appearance of these landmark articles, there has been explosive

growth of the number of publications about Blatter radicals, covering a wide range of research areas. Blatter radicals have been applied as photodetectors [7], emissive materials for OLEDs [8], and liquid crystal photoconductors [9,10] used in controllable polymerization reactions [11,12], molecular electronics [13], and molecular magnetism [14–19]. They are actively used as building blocks to construct magnetic bistable materials [17,20] and high-spin polyradicals and biradicaloids [21–23] or as organic paramagnetic ligands in hydride metal–radical complexes [24,25]. Moreover, Blatter-type radicals can be transferred via a vapor phase to create stable thin films (without degradation) while retaining their paramagnetic nature [26,27]. Active research is being conducted toward the creation and study of Blatter radical–inorganic “spin interfaces”, which may open up opportunities for using these radicals in spintronics devices [28–30]. As for comprehensive reviews, Zheng et al. summarized the synthesis, properties and specific role of Blatter radicals in devices and other technologies [31]. Coote et al. have discussed various methods to synthesize and customize Blatter radicals as well as their broad applications, including as sensors, spin labels, magnetic materials, liquid crystals and in polymer and small-molecule synthesis [32].

Owing to this broad interest in Blatter radicals, their chemistry has been systematically and successfully developed thereby considerably expanding structural diversity of Blatter radicals, bi- and polyradicals [33–36]. Special attention was given to the preparation of fluorinated derivatives of Blatter radicals [37]. For example, Koutentis et al. replaced the phenyl group at the C3 position in the Blatter heterocyclic system with a CF₃-group and revealed an abrupt spin transition for the radical at 58(2) K related to the phase transition [17]. In a series of other works, a trifluoromethyl group was introduced to the C7 position of the Blatter radical to give radicals with significantly improved chemical stability [38,39]. Herein, as part of our increasing interest in “structure–property” correlations inherent in fluorinated organic radicals [40–52], we report synthesis, structure and complete characterization of novel difluorophenyl-substituted Blatter radicals, namely 1-(3,4-difluorophenyl)-3-phenyl-1,4-dihydrobenzo[e][1,2,4]triazin-4-yl (**1a**) and 1-(2,4-difluorophenyl)-3-phenyl-1,4-dihydrobenzo[e][1,2,4]triazin-4-yl (**1b**).

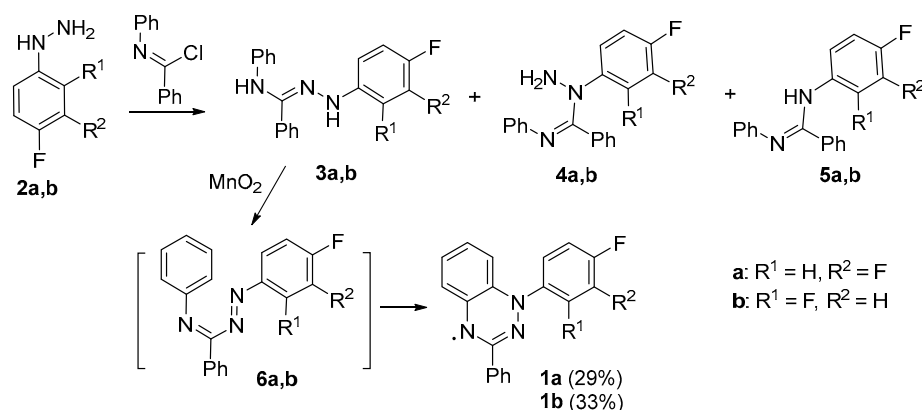
2. Results and Discussion

The syntheses of 1-(3,4-difluorophenyl)-(**1a**) and 1-(2,4-difluorophenyl)-3-phenyl-1,4-dihydrobenzo[e][1,2,4]triazin-4-yl (**1b**) were carried out via the classic route involving oxidation of amidrazones **3a,b** in situ, giving 1,2,4-triazabutadienes **6a,b**, which then underwent electrocyclic ring closure thus affording benzotriazines, which were next oxidized to the desired 1,2,4-benzotriazinyls **1a,b** (Scheme 1). Initial amidrazones **3a,b** were prepared by a reaction of corresponding arylhydrazines **2a,b** with *N*-phenylbenzimidoyl chloride [53]. The amidrazones **3a,b**, due to limited stability, were subjected to subsequent reactions without isolation. The yields of radicals **1a,b** were moderate because the syntheses of amidrazones **3a,b** were accompanied by the formation of corresponding backside products since the hydrazino group can attack via either the α or β nitrogen atom.

Analytically pure samples of 1,2,4-benzotriazinyls **1a,b** were obtained by column chromatography on silica gel, followed by procedures of recrystallization from a mixture of CH₂Cl₂ with *n*-heptane. Both 1,2,4-benzotriazinyls were comprehensively studied in solution and in the solid state.

Determination of electrochemical parameters of the processes of oxidation and reduction of 1,2,4-benzotriazinyls **1a,b** was carried out by cyclic voltammetry (CV) on a glassy carbon disc electrode in acetonitrile. It was found that radicals **1a,b** are oxidized and reduced chemically and electrochemically reversibly (Figures 1 and S1), which is typical of 1,2,4-benzotriazinyls [54–57]. This is evidenced by our analysis of the CV curves of oxidation and reduction obtained at potential sweep rates of 0.05–1.00 V/s (Figures 2, 3, S2 and S3). It was shown that for each process, the ratio of currents in the reverse and forward peaks does not depend on the potential sweep rate and is close to 1.0 (chemical reversibility), and that the value of the interval between the forward and reverse peaks lies in the range of

0.054–0.058 V and differs slightly from the theoretical value of 0.059 V for electrochemically reversible processes [58]. It is worth noting that 1,2,4-benzotriazinyl **1b** is oxidized and reduced at higher potentials ($E_{1/2}^{\text{ox}} = 0.336$ V and $E_{1/2}^{\text{red}} = -0.766$ V) as compared with derivative **1a** (0.295 and -0.709 V, respectively).



Scheme 1. Synthesis of 1-(3,4-difluorophenyl)-(1a) and 1-(2,4-difluorophenyl)-3-phenyl-1,4-dihydrobenzo[e][1,2,4]triazin-4-yl (1b). The reaction pathway is proposed in accordance with the literature mechanism [31].

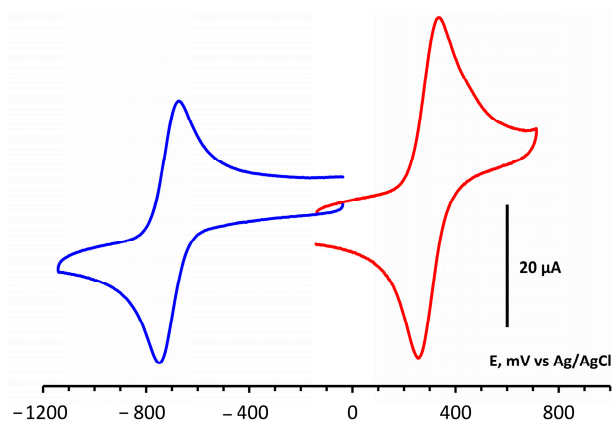


Figure 1. CV curves of oxidation (red) and reduction (blue) of **1a** (3×10^{-3} M) in 0.1 M $\text{Bu}_4\text{NBF}_4/\text{MeCN}$ on a glassy carbon disk electrode at a potential sweep rate of 0.1 V/s.

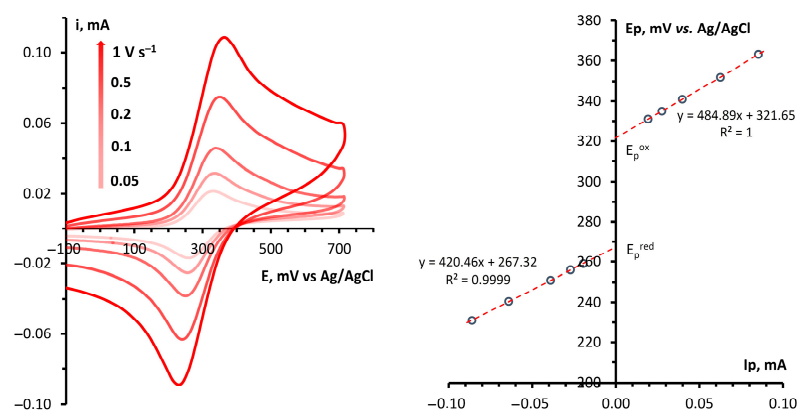


Figure 2. (left) CV curves of the oxidation of **1a** (3×10^{-3} M) in 0.1 M $\text{Bu}_4\text{NBF}_4/\text{MeCN}$ on a glassy carbon disk electrode at potential sweep rates of 0.05, 0.10, 0.20, 0.50, and 1.00 V/s. (right) Dependences of the potentials of the peaks of oxidation and reciprocal reduction on the current at the peak for the corresponding process.

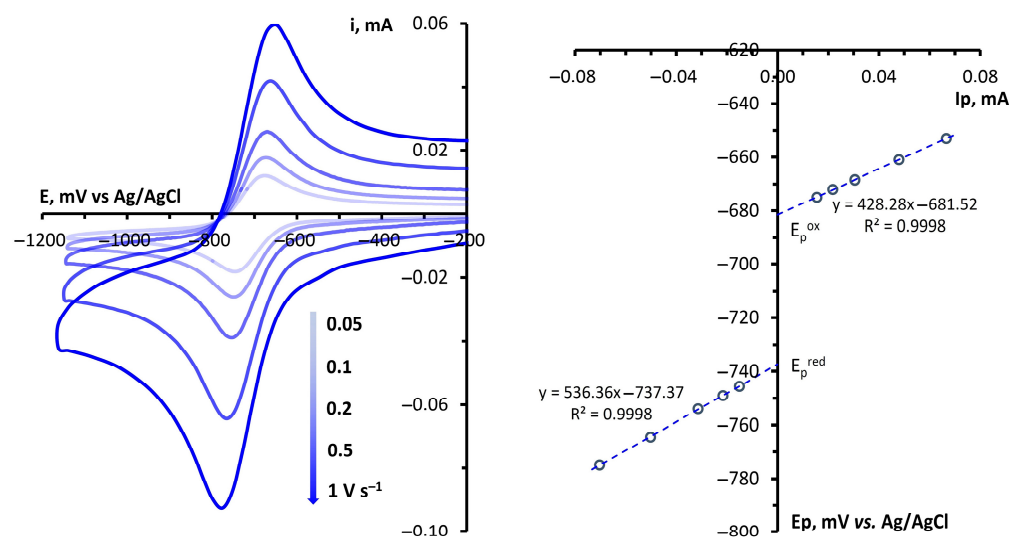


Figure 3. (left) CV curves of the reduction of **1a** (3×10^{-3} M) in 0.1 M $\text{Bu}_4\text{NBF}_4/\text{MeCN}$ on a glassy carbon disc electrode at potential sweep rates of 0.05, 0.10, 0.20, 0.50, and 1.00 V/s. (right) Plots of reduction and reciprocal oxidation peak potentials versus the peak current for the respective process.

Continuous-wave ESR spectra of 1,2,4-benzotriazinyls **1a,b** were recorded at room temperature in degassed toluene solutions of various concentrations. Dilute solutions of **1a,b** produced EPR spectra typical of Blatter radicals (Figure 4 and Figure S5), which consist of seven-line multiplets resulting from hyperfine interactions between an unpaired electron and three similar but slightly nonequivalent ^{14}N nuclei. The hyperfine coupling (HFC) constants and g_{iso} determined by the modeling of the EPR spectra and calculated at the UPBE0/def2-TZVP level are $a_{\text{N}(1)} = 0.73/0.57$, $a_{\text{N}(2)} = 0.49/0.41$, and $a_{\text{N}(4)} = 0.51/0.45$ mT with $g = 2.0040/2.0044$ in **1a** and $a_{\text{N}(1)} = 0.72/0.57$, $a_{\text{N}(2)} = 0.49/0.41$, and $a_{\text{N}(4)} = 0.51/0.45$ mT with $g = 2.0040/2.0044$ in **1b**. A comparison of the calculated HFC constants and Mulliken spin populations of N atoms indicated that they do not correlate, which can be explained by a slight deviation from the planarity of the triazinyl ring. The deviation leads to a small difference in the hybridization of the N atoms and therefore in populations of their s-type AOs.

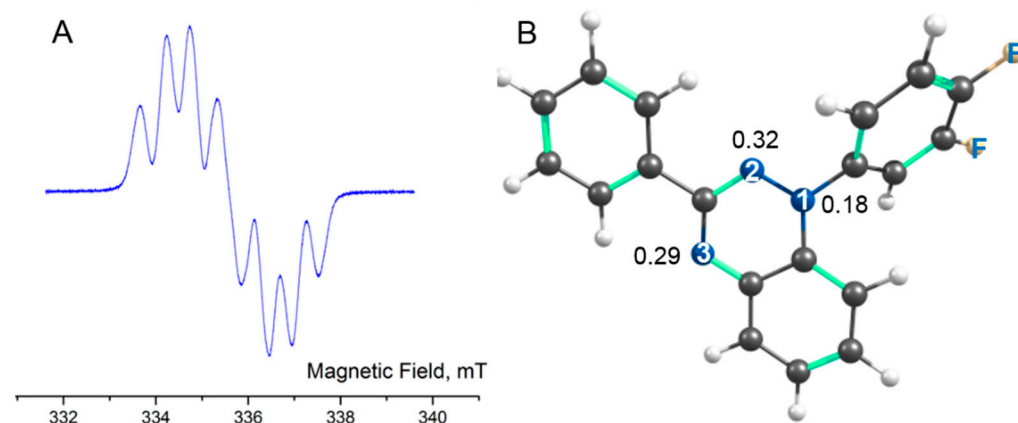


Figure 4. (A) The EPR spectrum of radical **1a** in a toluene solution ($\sim 10^{-5}$ M) at 298 K. (B) Optimized structure of **1a** with the numbering of nitrogen atoms and their Mulliken spin populations.

Figures 5 and S6 depict electronic absorption spectra of radicals **1a,b** in acetonitrile at room temperature. One can see that both paramagnets **1a,b** show rather strong absorption bands in the ultraviolet region with maxima at 268 and 266 nm, respectively. Other absorption bands in the near-UV and visible regions have substantially lower intensity; in

1a, the maxima of the bands are at 314, 369, 425, and 491, and there is a shoulder (sh.) at ~540 nm; and in **1b**, they are at 314, ~326 (sh.), 367, ~411 (sh.), ~454 (sh.), 486, and ~535 (sh.) nm. On the whole, the observed spectra are characteristic of related 1,2,4-benzotriazinyl radicals [59].

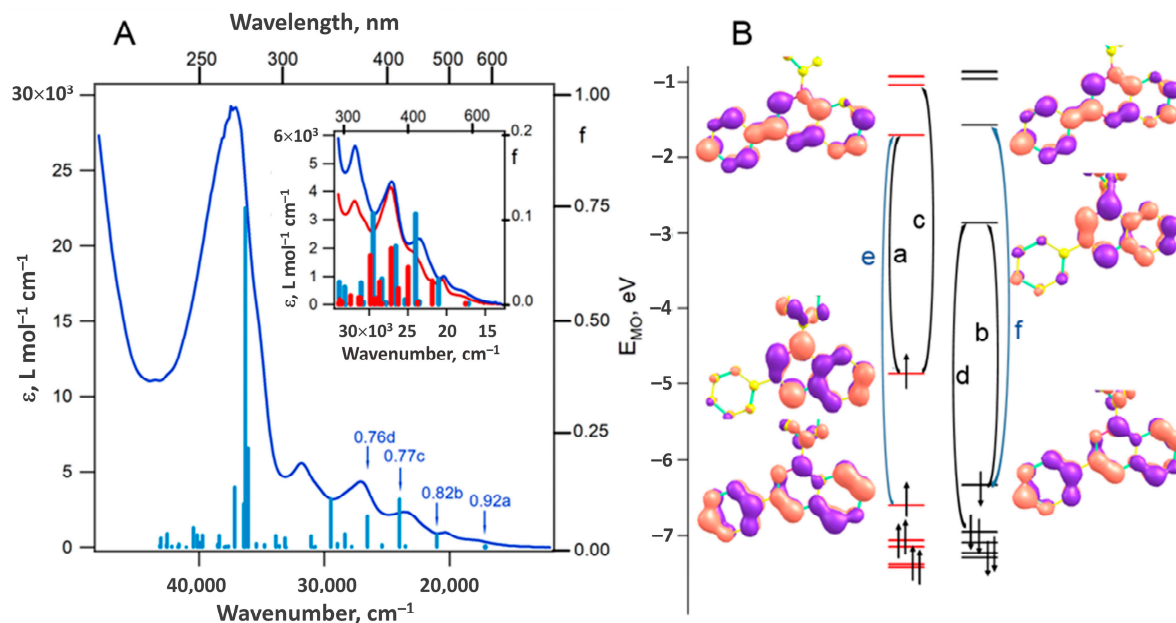


Figure 5. (A) The experimental electronic absorption spectrum of an acetonitrile solution of radical **1a** (10^{-4} M) (blue) recorded at room temperature [the inset shows enlarged spectra of **1a** (blue) and **1b** (red)] and the calculated positions and oscillator strengths (f) of the electronic transitions are depicted as blue bars for **1a** and as red bars for **1b**. (B) The diagram of α - (left) and β -type (right) molecular orbitals (MOs) calculated at the UB3LYP/def2-TZVP level for radical **1a** and selected electron transitions induced by UV and visible-light excitation as calculated by the TD-UB3LYP method with the same basis set (Table S1 presents all corresponding MOs).

Figure 5A shows that the results of the time-dependent DFT calculations are in good agreement with the experiment. According to the calculations, a series of 40 electronic transitions contributes to the UV-Vis spectra of radicals **1a** and **1b** in the range $17,000$ – $43,000$ cm^{-1} (~230–600 nm). At the same time, the near-UV and visible region ($17,000$ – $34,000$ cm^{-1} or ~295–600 nm) corresponds to excitations in approximately 20 excited states. Thus, the structure of this moderate-intensity absorption region is mainly related to the superposition of absorption bands onto different excited states. Nonetheless, the manifestation of vibrational structures of some bands could not be ruled out either.

Figure 5B displays a number of occupied and unoccupied molecular orbitals (MOs) in the ground state of **1a**. All MOs related to this diagram are presented in SI (Table S1). The letters a–f denote transitions of electrons between higher occupied and lower unoccupied MOs. According to the calculations, the main contribution (92%) to the lowest-energy excited state (Figure 5A) comes from the configuration with the promotion of the α -electron from SOMO to LUMO (excitation a). The main contribution (82%) to the second excited state comes from the promotion of the β -electron from HOMO to the SOMO counterpart (Figure 5B, excitation b). A similar description was also performed for transitions to the 4th and 6th excited states with the main contributions of promotions c and d (Figure 5A,B), respectively. Of note, the most intense transition at 275 nm ($f = 0.75$) matches excitations to the 21st excited state, whose wavefunction is the sum of a large number of configurations, the predominant of which correspond to the promotions of both α (e, 26%) or β (f, 20%) electrons from the HOMO to the LUMO (Figure 5B, excitations e and f).

The structures of radicals **1a,b** were successfully confirmed by single-crystal XRD. Figure 6 shows the structure of molecules **1a** and **1b** as a projection onto the plane of the bicyclic moiety. In structure **1a**, two crystallographically independent molecules **1aA** and **1aB** are similar in bond lengths but differ in the rotation of the plane of the nonfluorinated phenyl ring relative to the bicycle plane (Table 1); in **1aA**, this angle ($-22.8(3)^\circ$) is much larger than that in **1aB** ($5.0(3)^\circ$), whereas in **1b**, this angle has an intermediate value ($10.5(3)^\circ$). In **1aA** and **1aB**, the fluorinated ring forms angles 51 – 52° with the heterocyclic plane. By contrast, in **1b**, it is turned at almost the same angle in the opposite direction ($-58.3(2)^\circ$).

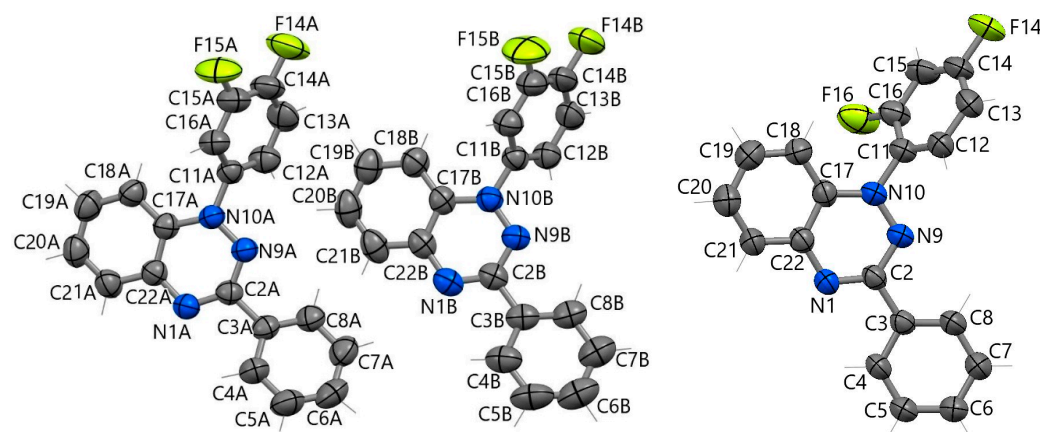


Figure 6. Structure of molecules **1aA** (left), **1aB** and **1b** (right) as a projection onto the heterocyclic-moiety plane and the atom numbering scheme. Parameters of atomic displacement are given with 50% probability (H atoms are omitted).

Table 1. Selected bond lengths, contacts (Å) and torsion angles ω (deg.) in **1a** and **1b**.

Bond	<i>d</i>		
	1aA	1aB	1b
N(1A)-C(2A)	1.330(2)	1.332(2)	1.333(2)
N(1A)-C(22A)	1.373(2)	1.366(2)	1.369(2)
C(2A)-N(9A)	1.332(2)	1.333(2)	1.337(2)
N(9A)-N(10A)	1.364(2)	1.358(2)	1.371(2)
N(10A)-C(17A)	1.386(2)	1.389(2)	1.385(2)
C(17A)-C(22A)	1.407(2)	1.412(2)	1.412(2)
Torsion angle	ω		
N(9)C(2)C(3)C(8)	$-22.8(3)$	$5.0(3)$	$10.5(3)$
N(9)N(10)C(11)C(12)	$51.2(2)$	$52.4(2)$	$-58.3(2)$
Contact	<i>d</i>		
N1B...C17B		3.351(3)	
N9B...C21B		3.444(3)	
N1A...C16A	3.427(3)		
(N...H-C)			
C4A...C12B'		3.449(3)	
N1A...N9B'		3.646(2)	
C12'...N9 (N...H-C)			3.377(3)
N1...C4			3.388(2)
C19...C22'			3.413(3)
N(9)...N(10')			3.784(2)

In radical **1a**, the shortest intermolecular contacts in the structures (less than 3.5 \AA) are shown in Figure 7. Alternating centrosymmetric dimers **1aA**...**1aA** and **1aB**...**1aB**

form stacks in the structure. Dimers $1aA \cdots 1aA$ arise due to H-bonds $C-H \cdots N$ [$C \cdots N$ 3.427(3) Å]. In $1aB \cdots 1aB$ dimers, the shortest distances between atoms of parallel bicyclic parts are 3.351(3) and 3.444(3) Å. Short $N \cdots N$ contacts of 3.646(2) Å can be seen between dimers (Figure 7). In structure $1b$, the parallel arrangement of bicyclic parts and phenyl rings favors the appearance of π -stacking interactions between them [the $C \cdots C$ and $C \cdots N$ distances are 3.413(3) and 3.388(2) Å, respectively], which are complemented by $C-H \cdots N$ hydrogen bonds [$C \cdots N$ 3.377(3) Å]. Considering these contacts, stacks of molecules can be distinguished in the structure of $1b$ (Figure 7).

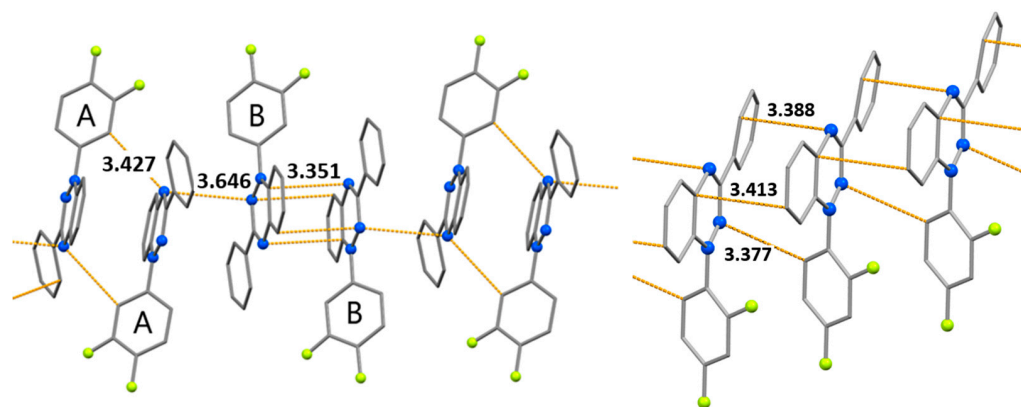


Figure 7. Fragments of stacks in crystal structures of radicals $1a$ (left) and $1b$ (right) with the shortest intermolecular contacts (H atoms are omitted). The letters A and B denote two crystallographically independent molecules $1aA$ and $1aB$, respectively.

To estimate the strength of exchange interactions between radicals and to select model magnetic motifs, parameters of exchange interactions within and between stacks were calculated using the spin-unrestricted broken-symmetry approach. This approach has previously been shown to work well for evaluating intermolecular exchange interactions [60,61]. In the case of $1a$, the stacks consist of two types of radicals, $1aA$ and $1aB$, with three types of contacts ($\cdots 1aA \cdots 1aA \cdots 1aB \cdots 1aB \cdots$). Therefore, in the calculations for $1a$, three considerably different parameters J were obtained (Table 2, $J_{1aA \cdots 1aA}$, $J_{1aA \cdots 1aB}$, and $J_{1aB \cdots 1aB}$) at a ratio of 1.00:0.12:0.61. In the case of $1b$, the structure consists of uniformly bound stacks with a single parameter, $J_{1b \cdots 1b}$. Table 2 indicates that $J_{1aA \cdots 1aA}$, $J_{1aB \cdots 1aB}$ and $J_{1b \cdots 1b}$ are of the same order of magnitude, while $J_{1aA \cdots 1aB}$ is much smaller. For both $1a$ and $1b$, our calculations predicted negligible exchange interactions between the radicals of neighboring stacks ($|J| \leq 0.2 \text{ cm}^{-1}$).

Table 2. Parameters of intrastack exchange interactions J calculated for crystal structures of $1a$ and $1b$ at the BS-UB3LYP/def2-TZVP level, and J values estimated from the best agreement between the simulation and experimental dependences of χT on T.

Radical	$1a$			$1b$
Parameter	$J_{1aA \cdots 1aA}$	$J_{1aA \cdots 1aB}$	$J_{1aB \cdots 1aB}$	$J_{1b \cdots 1b}$
$J_{\text{calc}}/\text{cm}^{-1}$	−116.6	−14.3	−70.5	−86.0
$J_{\text{calc}}/k_B, \text{K}$	−167.8	−20.6	−101.4	−123.7
$J_{\text{exp}}/k_B, \text{K}$	$−292 \pm 10$	—	—	$−222 \pm 17$

The temperature dependence of χT for radicals $1a$ and $1b$ is shown in Figure 8. For $1a$, χT at 300 K is $0.23 \text{ cm}^3 \text{ mol}^{-1} \text{K}$ and decreases with lowering temperature, reaching a plateau of $\sim 0.013 \text{ cm}^3 \text{ mol}^{-1} \text{K}$ below 60 K. The high-temperature value of χT is much lower than the theoretical spin-only value of $0.375 \text{ cm}^3 \text{ mol}^{-1} \text{K}$ for the noninteracting radicals at $g = 2$, and this finding indicates strong antiferromagnetic exchange interactions; the latter result is consistent with our calculations (Table 2). We simulated the dependence of χT

on T by means of a magnetic motif consisting of 12-membered radical stacks rolled into rings. To avoid overparametrization, we fixed the ratio of J values (1:0.12:0.61) obtained from the calculations. The following parameters correspond to the best fit: $g = 2.01 \pm 0.05$ and $J_{1aA...1aA}/k_B = -292 \pm 10$ K. Most likely, the nonzero value of χT below 60 K is due to a small amount of monomeric radicals ($\rho \approx 2.0\%$).

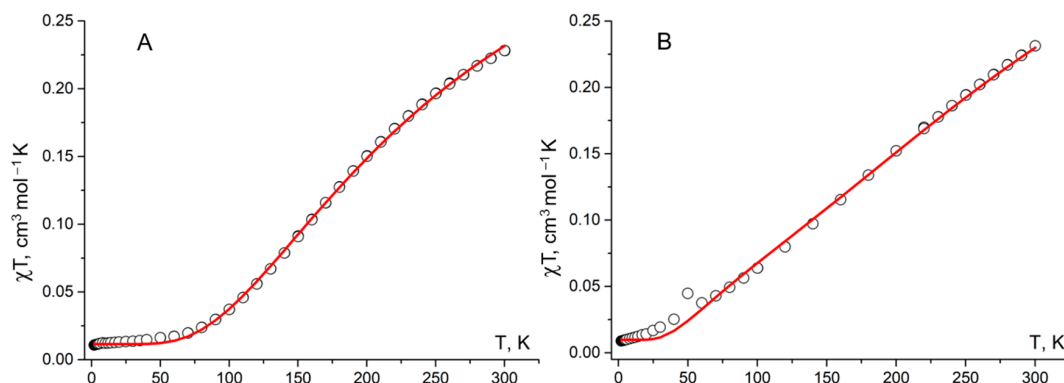


Figure 8. Temperature dependence of χT for radicals **1a** (A) and **1b** (B). Solid curves denote modeling with parameters presented in the text.

For **1b**, χT at 300 K is also $0.23 \text{ cm}^3 \text{ mol}^{-1} \text{ K}$ and diminishes with decreasing temperature to $0.009 \text{ cm}^3 \text{ mol}^{-1} \text{ K}$ at 2 K (Figure 8). Simulation of the dependence of χT on T with 12-membered looped uniform stacks yielded the following best-fit parameters: $J_{1b...1b}/k_B = -222 \pm 17$ K, $\rho \approx 2.0\%$, and $g = 2.04 \pm 0.01$.

Table 2 suggests that the results of BS-DFT calculations are in semiquantitative agreement with the parameters extracted from the simulation of the experimental temperature dependences of the molar magnetic susceptibility. This finding confirms the proposed magnetic motifs of crystals of radicals **1a** and **1b**.

Given that it was possible to solve crystal structures of difluoro derivatives **1a** and **1b**, it was reasonable to compare the structures of their solid phases (as well as magnetic properties) with those of nonfluorinated analog **1c** (CSD refcode: TICMOH [6,62]). According to single-crystal X-ray analysis, radicals **1c** are stacked along the b axis. In the columns, the phenyl ring at C3 and the 1,2,4-triazin-4(1H)-yl ring lie alternately one on top of the other (Figure 9). Within the array, the mean interplanar distance is 3.449 \AA , which can be considered the mean distance between adjacent π systems. Nevertheless, the centers of the 1,2,4-triazin-4(1H)-yl rings, bearing most of the spin population, are 5.50 \AA apart. Consequently, there are only very weak intermolecular interactions along the columns, in agreement with the results of static magnetic susceptibility measurements ($J_{1c...1c}/k_B = -2.2 \pm 0.2$ K) [5].

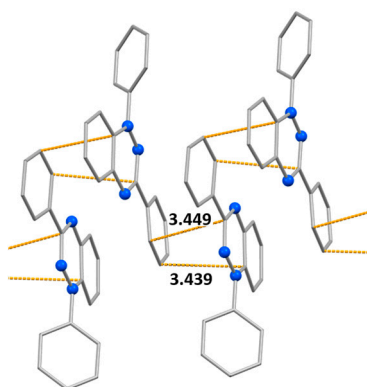


Figure 9. Fragments of crystal structures of radicals **1c** showing the columnar arrangement with the shortest intermolecular contacts (H atoms are omitted).

3. Conclusions

Thus, targeted synthesis of two isomeric Blatter's radicals, 1-(3,4-difluorophenyl)- (1a) and 1-(2,4-difluorophenyl)-3-phenyl-1,4-dihydrobenzo[e][1,2,4]triazin-4-yl (1b), was performed successfully. It was shown that the presence of two F atoms in the phenyl substituent has a substantial effect on the packing of radicals 1a and 1b and on their magnetic properties. Magnetic susceptibility analyses revealed that in both radicals, the radical-radical interactions are strong antiferromagnetic ($J/k_B = -292 \pm 10$ and -222 ± 17 K, respectively) due to an effective SOMO-SOMO overlap. The latter is related to peculiarities of the packing of the radicals, which in turn is predetermined by the electrostatic potential surfaces inherent in these paramagnetic molecules. This work shows that chemically, the electrostatic potential surface can be modulated efficiently by partial fluorination of the organic radicals, without expanding the geometry too much. To some extent, in the family of Blatter radicals, this approach may be an effective way to alter their structural properties in order to obtain materials with large magnetic couplings. Another important aspect that motivates further investigation into partly fluorinated Blatter radicals is that they possess an unprecedented combination of high thermal stability, reversibility of redox processes, and magnetic properties suitable for fabrication of magnetically active films, especially of double- and multi-layered films.

4. Experimental Part and Computational Details

4.1. Reagents and General Methods

All commercial reagents were used without further purification. Solvents were freshly distilled. All reaction mixtures and column eluents were monitored by thin-layer chromatography (TLC) using commercial silica gel 60 F254 precoated aluminum TLC plates (Merck KGaA, Darmstadt, Germany). The plates were visualized under UV radiation at 254 nm. Chromatography was performed on silica gel (0.063–0.200 mm) for column chromatography. Melting points were measured by means of Stuart melting point apparatus SMP 30; solvents used for recrystallization are indicated after the melting points.

Measurement of absorption spectra in the UV and visible range was carried out on an Agilent 8453 spectrometer (Agilent, Santa Clara, CA, USA) for 10^{-4} M solutions of compounds in acetonitrile, using a 10 mm quartz cuvette with a Teflon cap. IR spectra of samples in KBr were recorded on a BRUKER Vertex-70 FTIR spectrometer (Bruker Corporation, Billerica, MA, USA), and strong, medium and weak peaks are labeled as s, m and w, respectively. ^1H and ^{13}C NMR spectra were acquired on a Bruker Avance 300 spectrometer (Bruker Corporation, Billerica, MA, USA) at 300 and 75 MHz, respectively. Deuterated solvents were used to achieve a homonuclear lock, and the signals are presented in reference to the deuterated solvent peaks. Masses of molecular ions were determined by high-resolution mass spectrometry (HRMS) by means of a DFS Thermo Scientific instrument at an ionization energy of 70 eV (Thermo Fisher Scientific, Waltham, MA, USA). Elemental analyses were performed using a Euro EA 3000 elemental analyzer.

4.2. Syntheses

N-Phenylbenzimidoyl chloride [63]. In a round-bottom Schlenk flask, *N*-phenylbenzamide (3.0 g, 15.23 mmol) and SOCl_2 (8.85 mL, 8 eq.) were heated at 70 °C. After 4 h, the excess of SOCl_2 was removed to obtain the corresponding imidoyl chloride as a greenish solid (3.15 g, 96% yield), which was subjected to the next step without additional purification. The NMR results are in agreement with previously reported data. ^1H NMR (300 MHz, DMSO-d_6) δ 7.06–7.15 (m, 1 H), 7.30–7.41 (m, 2 H), 7.49–7.64 (m, 3 H), 7.78–7.86 (m, 2 H), 7.95–8.03 (m, 2 H). ^{13}C NMR (76 MHz, DMSO-d_6) δ 120.77, 124.07, 128.16, 128.82, 129.03, 131.99, 135.41, 139.59, and 165.93.

(3,4-Difluorophenyl)hydrazine. To a solution of 3,4-difluoroaniline (2 g, 15.59 mmol) in a mixture of water (6 mL) and concentrated HCl (12 M, 10 mL), we added dropwise a solution of NaNO_2 (1.18 g, 17.04 mmol) in water (2 mL) at 0–5 °C, and the reaction mixture was stirred at this temperature for 1 h. Then, a solution of SnCl_2 (8.74 g, 39.73 mmol) in

concentrated HCl (12 M, 7 mL) was introduced dropwise at 0–5 °C with vigorous stirring. The mixture was then allowed to warm up to room temperature and incubated for 30 min. The precipitate was filtered off, washed with Et₂O (5 mL), and dried in vacuo at 40 °C for 5 h, thus giving (3,4-difluorophenyl)hydrazine hydrochloride as a pale brown solid. Next, the salt was treated with a 40% aqueous NaOH solution (10 mL), and the product was extracted with CH₂Cl₂ (2 × 5 mL). The combined organic layers were dried over Na₂SO₄ and concentrated in vacuo to obtain the desired products. Yield 1.69 g (75%), yellow crystals. The product was used at the next reaction step without purification.

(2,4-Difluorophenyl)hydrazine [64]. To a solution of aniline (2 g, 15.59 mmol) in a mixture of water (6 mL) and concentrated HCl (12 M, 10 mL), a solution of NaNO₂ (1.18 g, 17.04 mmol) in water (2 mL) was added dropwise at 0–5 °C, and the reaction mixture was stirred at this temperature for 1 h. Then, a solution of SnCl₂ (8.74 g, 39.73 mmol) in concentrated HCl (12 M, 7 mL) was introduced dropwise at 0–5 °C with vigorous stirring. The mixture was then warmed to room temperature and incubated for 30 min. The precipitate was filtered off, washed with Et₂O (5 mL), and dried in vacuo at 40 °C for 5 h, thereby affording (2,4-difluorophenyl)hydrazine hydrochloride as a violet solid. The salt was treated with a 40% aqueous NaOH solution (10 mL), and the mixture was extracted with CH₂Cl₂ (2 × 5 mL) to obtain the title product. Yield 1.69 g (75%), dark yellow crystals, and mp 59–61 °C. The product was subjected to the next reaction step without purification.

N'-(3,4-Difluorophenyl)-*N''*-phenylbenzohydrazonamide (**3a**) or *N'*-(2,4-difluorophenyl)-*N''*-phenylbenzohydrazonamide (**3b**). *N*-phenylbenzimidoyl chloride (0.3 g, 0.98 mmol) was added to a stirred solution of (3,4-difluorophenyl)hydrazine or (2,4-difluorophenyl)hydrazine (0.478 g, 2.22 mmol) and Et₃N (0.336 g, 3.32 mmol) in dry THF (3 mL) at –10 °C. red at 0 °C for 8 h. The solvent was evaporated under reduced pressure, the residue was treated with a 2% aqueous acetic acid solution (10 mL), and the organic products were extracted with CH₂Cl₂. The combined extracts were dried with Na₂SO₄, and the solvent was evaporated. Crude products **3a** or **3b** were partially purified by flash chromatography (SiO₂, hexane/CH₂Cl₂, 3:1), and due to limited stability, were quickly subjected to subsequent reactions. Note that in one of the experiments crystals of compound **3a** were obtained by chance that allowed to solve its molecular and crystal structure (see Section 4.5).

1-(3,4-Difluorophenyl)-3-phenyl-1,4-dihydrobenzo[*e*][1,2,4]triazin-4-yl (**1a**). MnO₂ (0.81 g, 9.32 mmol) was added to a stirred solution of amidrazone **3a** (0.3 g, 0.93 mmol) in dry CH₂Cl₂ (4 mL), then the reaction mixture was stirred for 6 h at room temperature. After evaporation of the solvent, the crude product was purified by column chromatography (petroleum ether/ethyl acetate [9:1], *R_f* = 0.72). Yield 0.086 g (29%), crystals of dark-brown color, and mp 110.2–110.7 °C (from a mixture of CH₂Cl₂ with *n*-heptane). IR (KBr): 3447 (m), 3058 (w), 2958 (w), 2927 (w), 2857 (w), 1728 (m), 1613 (m), 1513 (s), 1484 (s), 1450 (m), 1393 (s), 1328 (m), 1268 (m), 1203 (m), and 1175 (w) cm^{–1}. EPR (toluene): *g* = 2.0040; *a_{N(1)}* = 0.73, *a_{N(4)}* = 0.51, and *a_{N(2)}* = 0.49 mT. HRMS (ESI): *m/z* [M]⁺ calcd for C₁₉H₁₂F₂N₃ 320.0999, found 320.1002. Found, %: C, 71.37; H, 3.64; F, 11.39; and N, 13.07. Calcd. for C₁₉H₁₂F₂N₃, %: C, 71.24; H, 3.78; F, 11.86; and N, 13.12.

1-(2,4-Difluorophenyl)-3-phenyl-1,4-dihydrobenzo[*e*][1,2,4]triazin-4-yl (**1b**). MnO₂ (0.81 g, 9.32 mmol) was added to a stirred solution of amidrazone **3b** (0.3 g, 0.93 mmol) in dry CH₂Cl₂ (4 mL), then the reaction mixture was stirred for 6 h at room temperature. After evaporation of the solvent, the crude product was purified by column chromatography (petroleum ether/ethyl acetate [9:1], *R_f* = 0.68). Yield 0.098 g (33%), swamp-colored crystals, and mp 128.6–129.2 °C (from a mixture of CH₂Cl₂ with *n*-heptane). IR (KBr): 3471 (m), 3062 (w), 3030 (w), 1947 (w), 1877 (w), 1610 (s), 1508 (s), 1483 (s), 1452 (m), 1431 (m), 1395 (s), 1347 (w), 1269 (m), 1229 (m), 1203 (w), and 1141 (m) cm^{–1}. EPR (toluene): *g* = 2.0040; *a_{N(1)}* = 0.72, *a_{N(4)}* = 0.51, and *a_{N(2)}* = 0.49 mT. HRMS (ESI): *m/z* [M]⁺ calcd for C₁₉H₁₂F₂N₃ 320.0999, found 320.0998. Found, %: C, 71.64; H, 3.52; F, 11.41; and N, 13.10. Calcd. for C₁₉H₁₂F₂N₃, %: C, 71.24; H, 3.78; F, 11.86; and N, 13.12.

4.3. EPR Spectroscopy

EPR measurements were carried out on a Jeol JES-FA200 X-band spectrometer (Akishima, Tokyo 196-8558, Japan) using a Jeol X-Band Microwave Unit (9.8 GHz) at 290 K in dilute (down to approximately 10^{-5} M) toluene solutions degassed by argon bubbling. The spectra were recorded during one slow (~1 h) scan with a modulation of 0.2 mT at 100 kHz and a power of 4 MW. Isotropic g-factor values were measured experimentally using MgO doped with Mn(II) ions as a standard placed in the resonator simultaneously with the test solution. The spectra were simulated in Winsim v.0.96 software [65]. Estimated accuracy of determination of HFS constants and of the g value was 0.005 mT and 0.0001, respectively.

4.4. CV

CV measurements were performed in a dry glove box with an argon atmosphere and humidity and oxygen levels not exceeding 1 ppm. The analyzed compounds dissolved in acetonitrile (10^{-4} M) were subjected to electrochemical transformations in a standard three-electrode glass cell at a potential sweep rate of 0.05–1.00 V·s⁻¹. The working electrode was a glassy carbon disc electrode with a diameter of 2.7 mm. Before use, its surface was polished with sandpaper and then by means of chromium (III) oxide paste to achieve a mirror finish. The auxiliary electrode was a platinum wire calcined in a gas burner flame to remove oxides and other possible contaminants from the surface. Potentials of the studied processes were measured relative to a reference electrode, which was a silver wire coated with a layer of silver chloride, separated from the bulk of the electrolyte by an electrolytic bridge filled with a solution of the supporting electrolyte. The reference electrode was calibrated against a ferrocene/ferrocenium couple ($E^0 = 0.640$ V with respect to SHE). The supporting electrolyte was a 0.1 M solution of Bu₄NBF₄ (99%, Sigma-Aldrich, Burlington, MA, USA) in acetonitrile, ≥99.9%, HPLC gradient grade (Fisher Chemical, Loughborough, UK) with water content not exceeding 20 ppm, according to Karl Fischer titration; Mettler-Toledo titrator C10SD was employed.

4.5. Single-Crystal X-ray Diffractometry

XRD data on single crystals of **1a**, **1b**, and **3a** were collected on a Bruker AXS diffractometer, an Apex Duo (Cu K α , $\lambda = 1.54178$ Å, room temperature). In addition, XRD data on a single crystal of **3a** were collected at 100 K on a Bruker D8 QUEST diffractometer. Single-crystal X-ray analyses were carried out in the APEX3 software [66]. Absorption correction was applied by means of Bruker SADABS (version 2.10) [67]. The structure was solved by direct methods and refined by the full-matrix least-squares method in an anisotropic approximation for all nonhydrogen atoms. Positions of the H atoms were calculated geometrically and included in the refinement in a riding model. All calculations for structure solution and refinement were performed in SHELXL-2018/3 [68,69].

Crystallographic data were deposited with the Cambridge Crystallographic Data Centre and can be obtained free of charge via <http://www.ccdc.cam.ac.uk/conts/retrieving.html>, accessed on 28 July 2023 (or from the CCDC, 12 Union Road, Cambridge CB2 1EZ, UK; Fax: +44-1223-336033; E-mail: deposit@ccdc.cam.ac.uk).

Crystallographic data for **1a**: C₁₉H₁₂F₂N₃, $M = 320.32$, $T = 296$ K, triclinic space group $P-1$, $a = 10.090(3)$, $b = 13.144(3)$, $c = 13.207(4)$ Å, $\alpha = 75.170(15)$, $\beta = 89.178(15)$, $\gamma = 67.551(14)^\circ$, $V = 1558.0(7)$ Å³; $Z = 4$, $\rho_{\text{calc}} = 1.366$ g·cm⁻³, $\mu(\text{Cu K}\alpha) = 0.829$ mm⁻¹, θ range 3.477–68.110°, I_{hkl} collected/unique 13,490/5451, $R_{\text{int}} = 0.0582$, 3797 I_{hkl} with $I > 2\sigma(I)$, 542 refined parameters, $\text{Goof} = 1.059$, $R_1 = 0.0458$, $wR_2 = 0.1357$, and CCDC 2253805.

Crystallographic data for **1b**: C₁₉H₁₂F₂N₃, $M = 320.32$, $T = 296$ K, monoclinic space group $C2/c$, $a = 24.2137(14)$, $b = 4.3811(3)$, $c = 29.4449(19)$ Å, $\beta = 106.403(4)^\circ$, $V = 2996.5(3)$ Å³; $Z = 8$, $\rho_{\text{calc}} = 1.420$ g·cm⁻³, $\mu(\text{Cu K}\alpha) = 0.863$ mm⁻¹, θ range 3.806–66.727°, I_{hkl} collected/unique 9767/2575, $R_{\text{int}} = 0.0464$, 1800 I_{hkl} with $I > 2\sigma(I)$, 217 refined parameters, $\text{Goof} = 1.030$, $R_1 = 0.0451$, $wR_2 = 0.1235$, and CCDC 2253804.

Crystallographic data for **3a**: C₁₉H₁₃F₂N₃, $M = 321.32$, $T = 296$ K, orthorhombic space group $Pbca$, $a = 19.7195(10)$, $b = 7.2781(4)$, $c = 22.1358(12)$ Å, $V = 3176.9(3)$ Å³; $Z = 8$,

$\rho_{\text{calc}} = 1.344 \text{ g}\cdot\text{cm}^{-3}$, $\mu(\text{Cu K}\alpha) = 0.81 \text{ mm}^{-1}$, θ range 3.994–67.832°, I_{hkl} collected/unique 18,569/2871, $R_{\text{int}} = 0.0526$, 2379 I_{hkl} with $I > 2\sigma(I)$, 269 refined parameters, $\text{Goof} = 1.030$, $R_1 = 0.0572$, $wR_2 = 0.1690$, and CCDC 2285424.

Crystallographic data for **3a**: $\text{C}_{19}\text{H}_{13}\text{F}_2\text{N}_3$, $M = 320.32$, $T = 100 \text{ K}$, orthorhombic space group $Pbca$, $a = 19.6798(5)$, $b = 7.0705(2)$, $c = 22.0254(6) \text{ \AA}$, $V = 3064.75(14) \text{ \AA}^3$; $Z = 6$, $\rho_{\text{calc}} = 1.393 \text{ g}\cdot\text{cm}^{-3}$, $\mu(\text{Mo K}\alpha) = 0.101 \text{ mm}^{-1}$, θ range 2.070–30.582°, I_{hkl} collected/unique 19,008/4684, $R_{\text{int}} = 0.0318$, 4029 I_{hkl} with $I > 2\sigma(I)$, 218 refined parameters, $\text{Goof} = 0.918$, $R_1 = 0.0431$, $wR_2 = 0.1147$, and CCDC 2285423.

4.6. Magnetic Measurements

Magnetic susceptibility of the polycrystalline samples was measured with a Quantum Design MPMSXL SQUID magnetometer in the temperature range 2–300 K in a magnetic field of up to 5 kOe. Diamagnetic corrections were made using the Pascal constants.

4.7. Computational Details

Parameters of exchange interactions ($\hat{H} = -2 \sum J_{ij} \hat{S}_i \hat{S}_j$) between radicals were calculated via the spin-unrestricted broken-symmetry approach [70] and the Yamaguchi formula [71]

$$J = -\frac{E^{HS} - E_{BS}^{LS}}{\langle S^2 \rangle^{HS} - \langle S^2 \rangle_{BS}^{LS}}$$

where the energies of the high-spin (HS) and low-spin (LS) states were calculated at the UB3LYP/def2-TZVP [72–74] level for XRD geometry of radical pairs.

Geometries of **1a** and **1b** optimized at the B97-D3/def2-SVP [75–77] level in acetonitrile and toluene were used to calculate the EPR parameters (g_{iso} and HFC constants with ^{14}N) as well as the energies and oscillator strengths of electronic transitions in the UV-Vis spectra. The solvent was taken into account using the CPCM model [78]. The EPR parameters were computed at the PBE0/def2-TZVP level [79]. The UV/Vis spectra of radicals **1a** and **1b** were calculated via the time-dependent DFT approach [80] with the B3LYP functional and the def2-TZVP basis set.

All calculations were performed using the ORCA 5.0.1 software package [81].

To simulate the temperature dependence of the molar magnetic susceptibility, $\chi(T)$, in the form of product $\chi(T) \times T$, we utilized custom-designed software [82]. For both radicals, the magnetic motifs consist of stacks of exchange-coupled radicals. In the case of **1b**, these are uniformly bound stacks. For **1a**, the situation is more complicated: the stacks consist of two types of molecules, **1aA** and **1aB**, with three types of contacts ($\cdots\mathbf{1aA}\cdots\mathbf{1aA}\cdots\mathbf{1aB}\cdots\mathbf{1aB}\cdots$), and consequently, there are three different J parameters ($J_{\mathbf{1aA}\cdots\mathbf{1aA}}$, $J_{\mathbf{1aA}\cdots\mathbf{1aB}}$, and $J_{\mathbf{1aB}\cdots\mathbf{1aB}}$). To avoid overparametrization, the ratio of these parameters was fixed based on the calculation results (Table 2).

Supplementary Materials: The following supporting information can be downloaded at: <https://www.mdpi.com/article/10.3390/catal13081206/s1>, Figure S1. CV curves of oxidation and reduction of **1b** ($3 \times 10^{-3} \text{ M}$) in 0.1 M $\text{Bu}_4\text{NBF}_4/\text{MeCN}$ on a glassy carbon disk electrode at a potential sweep rate of 0.1 V/s; Figure S2. (left) CV curves of the oxidation of **1b** ($3 \times 10^{-3} \text{ M}$) in 0.1 M $\text{Bu}_4\text{NBF}_4/\text{MeCN}$ on a glassy carbon disk electrode at potential sweep rates of 0.05, 0.10, 0.20, 0.50, and 1.00 V/s. (right) Dependences of the potentials of the peaks of oxidation and reciprocal reduction on the current at the peak for the corresponding process; Figure S3. CV curves of reduction of **1b** ($3 \times 10^{-3} \text{ M}$) in 0.1 M $\text{Bu}_4\text{NBF}_4/\text{MeCN}$ on a glassy carbon disc electrode at potential sweep rates of 0.05, 0.10, 0.20, 0.50, and 1.00 V/s. (right) Plots of reduction and reciprocal oxidation peak potentials versus peak current for the respective process; Figure S4. The EPR spectrum of radical **1a** (black) in toluene solution ($\sim 10^{-5} \text{ M}$) at 298 K and its modeling (red); Figure S5. The EPR spectrum of radical **1b** (black) in toluene solution ($\sim 10^{-5} \text{ M}$) at 298 K and its modeling (red); Figure S6. The experimental electronic absorption spectrum of an acetonitrile solution of radical **1b** (10^{-4} M) recorded at room temperature [the inset shows enlarged spectra of **1b**]; Table S1. A series of higher occupied and lower unoccupied MOs of α and β type and their energies for radical **1a**.

Author Contributions: Conceptualization, E.T. and N.P.G.; investigation, D.G., A.S., A.A., D.E.G., S.V.M., G.R. and A.B.; formal analysis, A.A., G.R. and A.B.; supervision, M.S. and E.T.; writing—original draft preparation, E.T. and N.P.G. All authors have read and agreed to the published version of the manuscript.

Funding: D.G. (Dmitry Gorbunov), S.M. and N.G. acknowledge the core funding from the Russian Federal Ministry of Science and Higher Education (FWGF-2021-0002) and the Research Resource Center “Irkutsk Supercomputer Center SB RAS” for the computational resources. The authors wish to thank A. Korlyukov (INEOS RAS) for single crystal analyses of **3a** at 100 K.

Data Availability Statement: The data presented in this study are available in this article.

Conflicts of Interest: The authors declare no conflict of interest.

References

1. Blatter, H.M.; Lukaszewski, H. A new stable free radical. *Tetrahedron Lett.* **1968**, *9*, 2701–2705. [[CrossRef](#)]
2. Neugebauer, F.A.; Umminger, I. 1,4-Dihydro-1,2,4-benzotriazin-Radikalkationen. *Chem. Berichte* **1981**, *114*, 2423–2430. [[CrossRef](#)]
3. Kadirov, M.K.; Il'yasov, A.V.; Vafina, A.A.; Buzykin, B.I.; Gazetdinova, N.G.; Kitaev, Y.P. Double electron-nuclear resonance of free radical 1,3-diphenyl-1, 4-dihydro-1,2,4-benzotriazin-4-yl. *Russ. Chem. Bull.* **1984**, *33*, 649–650. [[CrossRef](#)]
4. Hutchison, K.A.; Srdanov, G.; Menon, R.; Gabriel, J.-C.P.; Knight, B.; Wudl, F. A Pressure Sensitive Two-Dimensional Tetracyanoquinodimethane (TCNQ) Salt of a Stable Free Radical. *J. Am. Chem. Soc.* **1996**, *118*, 13081–13082. [[CrossRef](#)]
5. Mukai, K.; Inoue, K.; Achiwa, N.; Jamali, J.B.; Krieger, C.; Neugebauer, F.A. Magnetic-properties of 1,4-dihydro-1,2,4-benzotriazin-4-yl radicals. *Chem. Phys. Lett.* **1994**, *224*, 569–575. [[CrossRef](#)]
6. Krieger, C.; Neugebauer, F.A. Columnar Stacking of 1,3-Diphenyl-1,2,4-benzotriazin-4(1H)-yl Radicals. *Acta Crystallogr. C* **1996**, *52*, 3124–3126. [[CrossRef](#)]
7. Zheng, Y.; Miao, M.S.; Dantelle, G.; Eisenmenger, N.D.; Wu, G.; Yavuz, I.; Chabynec, M.L.; Houk, K.N.; Wudl, F. A solid-state effect responsible for an organic quintet state at room temperature and ambient pressure. *Adv. Mater.* **2015**, *27*, 1718–1723. [[CrossRef](#)]
8. Karecla, G.; Papagiorgis, P.; Panagi, N.; Zissimou, G.A.; Constantinides, C.P.; Koutentis, P.A.; Itskos, G.; Hayes, S.C. Emission from the stable Blatter radical. *New J. Chem.* **2017**, *41*, 8604–8613. [[CrossRef](#)]
9. Jasiński, M.; Szczytko, J.; Pocięcha, D.; Monobe, H.; Kaszyński, P. Substituent-Dependent Magnetic Behavior of Discotic Benzo[e][1,2,4]triazinyls. *J. Am. Chem. Soc.* **2016**, *138*, 9421–9424. [[CrossRef](#)]
10. Jasiński, M.; Kapuściński, S.; Kaszyński, P. Stability of a columnar liquid crystalline phase in isomeric derivatives of the 1,4-dihydrobenzo[e][1,2,4]triazin-4-yl: Conformational effects in the core. *J. Mol. Liq.* **2019**, *277*, 1054–1059. [[CrossRef](#)]
11. Areephong, J.; Mattson, K.M.; Treat, N.J.; Poelma, S.O.; Kramer, J.W.; Sprafke, H.A.; Latimer, A.A.; de Alaniz, J.R.; Hawker, C.J. Triazine-mediated controlled radical polymerization: New unimolecular initiators. *Polym. Chem.* **2015**, *7*, 370–374. [[CrossRef](#)]
12. Demetriou, M.; Berezin, A.A.; Koutentis, P.A.; Krasia-Christoforou, T. Benzotriazinyl-mediated controlled radical polymerization of styrene. *Polym. Int.* **2014**, *63*, 674–679. [[CrossRef](#)]
13. Zhang, Y.; Zheng, Y.; Zhou, H.; Miao, M.S.; Wudl, F.; Nguyen, T.Q. Temperature Tunable Self-Doping in Stable Diradicaloid Thin-Film Devices. *Adv. Mater.* **2015**, *27*, 7412–7419. [[CrossRef](#)]
14. Shu, C.; Pink, M.; Junghoefer, T.; Nadler, E.; Rajca, S.; Casu, M.B.; Rajca, A. Synthesis and Thin Films of Thermally Robust Quartet ($S = 3/2$) Ground State Triradical. *J. Am. Chem. Soc.* **2021**, *143*, 5508–5518. [[CrossRef](#)] [[PubMed](#)]
15. Miura, Y.; Yoshioka, N. p-Stacked structure of thiadiazolo-fused benzotriazinyl radical: Crystal structure and magnetic properties. *Chem. Phys. Lett.* **2015**, *626*, 11–14. [[CrossRef](#)]
16. Zheng, Y.; Miao, M.; Kemei, M.C.; Seshadri, R.; Wudl, F. The Pyreno-Triazinyl Radical-Magnetic and Sensor Properties. *Isr. J. Chem.* **2014**, *54*, 774–778. [[CrossRef](#)]
17. Constantinides, C.P.; Berezin, A.A.; Zissimou, G.A.; Manoli, M.; Leitius, G.M.; Bendikov, M.; Probert, M.R.; Rawson, J.M.; Koutentis, P.A. A magnetostructural investigation of an abrupt spin transition for 1-phenyl-3-trifluoromethyl-1,4-dihydrobenzo[e][1,2,4]triazin-4-yl. *J. Am. Chem. Soc.* **2014**, *136*, 11906–11909. [[CrossRef](#)]
18. Yan, B.; Cramen, J.; McDonald, R.; Frank, N.L. Ferromagnetic spin-delocalized electron donors for multifunctional materials: P-conjugated benzotriazinyl radicals. *Chem. Commun.* **2011**, *47*, 3201–3203. [[CrossRef](#)]
19. Takahashi, Y.; Miura, Y.; Yoshioka, N. Synthesis and properties of the 3-tert-butyl-7-trifluoromethyl-1,4-dihydro-1-phenyl-1,2,4-benzotriazin-4-yl radical. *New J. Chem.* **2015**, *39*, 4783–4789. [[CrossRef](#)]
20. Takahashi, Y.; Tsuchiya, N.; Miura, Y.; Yoshioka, N. Magneto-structural correlation of cyano-substituted 3-tert-butyl-1-phenyl-1,2,4-benzotriazin-4-yl: Spin transition behaviour observed in a 6-cyano derivative. *New J. Chem.* **2018**, *42*, 9949–9955. [[CrossRef](#)]
21. Hu, X.; Zhao, L.; Chen, H.; Ding, Y.; Zheng, Y.-Z.; Miao, M.-S.; Zheng, Y. Air stable high-spin blatter diradicals: Non-Kekulé versus Kekulé structures. *J. Mater. Chem. C* **2019**, *7*, 6559–6563. [[CrossRef](#)]
22. Gallagher, N.M.; Bauer, J.J.; Pink, M.; Rajca, S.; Rajca, A. High-Spin Organic Diradical with Robust Stability. *J. Am. Chem. Soc.* **2016**, *138*, 9377–9380. [[CrossRef](#)]
23. Gallagher, N.; Zhang, H.; Junghoefer, T.; Giangrisostomi, E.; Ovsyannikov, R.; Pink, M.; Rajca, S.; Casu, M.B.; Rajca, A. Thermally and Magnetically Robust Triplet Ground State Diradical. *J. Am. Chem. Soc.* **2019**, *141*, 4764–4774. [[CrossRef](#)] [[PubMed](#)]

24. Morgan, I.S.; Mansikkamäki, A.; Zissimou, G.A.; Koutentis, P.A.; Rouzières, M.; Clérac, R.; Tuononen, H.M. Coordination Complexes of a Neutral 1,2,4-Benzotriazinyl Radical Ligand: Synthesis, Molecular and Electronic Structures, and Magnetic Properties. *Chem. Eur. J.* **2015**, *21*, 15843–15853. [[CrossRef](#)] [[PubMed](#)]
25. Morgan, I.S.; Mansikkamäki, A.; Rouzières, M.; Clérac, R.; Tuononen, H.M. Coexistence of long-range antiferromagnetic order and slow relaxation of the magnetization in the first lanthanide complex of a 1,2,4-benzotriazinyl radical. *Dalton Trans.* **2017**, *46*, 12790–12793. [[CrossRef](#)] [[PubMed](#)]
26. Ciccullo, F.; Gallagher, N.M.; Geladari, O.; Chassé, T.; Rajca, A.; Casu, M.B. A Derivative of the Blatter Radical as a Potential Metal-Free Magnet for Stable Thin Films and Interfaces. *ACS Appl. Mater. Interfaces* **2016**, *8*, 1805–1812. [[CrossRef](#)] [[PubMed](#)]
27. Casu, M.B. Nanoscale Studies of Organic Radicals: Surface, Interface, and Spinterface. *Acc. Chem. Res.* **2018**, *51*, 753–760. [[CrossRef](#)]
28. Low, J.Z.; Kladnik, G.; Patera, L.L.; Sokolov, S.; Lovat, G.; Kumarasamy, E.; Repp, J.; Campos, L.M.; Cvetko, D.; Morgante, A.; et al. The Environment-Dependent Behavior of the Blatter Radical at the Metal–Molecule Interface. *Nano Lett.* **2019**, *19*, 2543–2548. [[CrossRef](#)]
29. Patera, L.L.; Sokolov, S.; Low, J.Z.; Campos, L.M.; Venkataraman, L.; Repp, J. Resolving the Unpaired-Electron Orbital Distribution in a Stable Organic Radical by Kondo Resonance Mapping. *Angew. Chem. Int. Ed.* **2019**, *58*, 11063–11067. [[CrossRef](#)]
30. Ciccullo, F.; Calzolari, A.; Bader, K.; Neugebauer, P.; Gallagher, N.M.; Rajca, A.; van Slageren, J.; Casu, M.B. Interfacing a Potential Purely Organic Molecular Quantum Bit with a Real-Life Surface. *ACS Appl. Mater. Interfaces* **2019**, *11*, 1571–1578. [[CrossRef](#)]
31. Ji, Y.; Long, L.; Zheng, Y. Recent advances of stable Blatter radicals: Synthesis, properties and applications. *Mater. Chem. Front.* **2020**, *4*, 3433–3443. [[CrossRef](#)]
32. Rogers, F.J.M.; Norcott, P.L.; Coote, M.L. Recent advances in the chemistry of benzo[e][1,2,4]triazinylradicals. *Org. Biomol. Chem.* **2020**, *18*, 8255–8277. [[CrossRef](#)] [[PubMed](#)]
33. Berezin, A.A.; Zissimou, G.; Constantinides, C.P.; Beldjoudi, Y.; Rawson, J.M.; Koutentis, P.A. Route to Benzo- and Pyrido-Fused 1,2,4-Triazinyl Radicals via *N'*-(Het)aryl-*N'*-[2-nitro(het)aryl]hydrazides. *J. Org. Chem.* **2014**, *79*, 314–327. [[CrossRef](#)] [[PubMed](#)]
34. Savva, A.C.; Mirallai, S.I.; Zissimou, G.A.; Berezin, A.A.; Demetriades, M.; Kourtellaris, A.; Constantinides, C.P.; Nicolaidis, C.; Trypinotis, T.; Koutentis, P.A. Preparation of Blatter Radicals via Aza-Wittig Chemistry: The Reaction of *N*-Aryliminophosphoranes with 1-(Het)aroyl-2-aryldiazenes. *J. Org. Chem.* **2017**, *82*, 7564–7575. [[CrossRef](#)] [[PubMed](#)]
35. Constantinides, C.P.; Obijalska, E.; Kaszynski, P. Access to 1,4-Dihydrobenzo[e][1,2,4]triazin-4-yl Derivatives. *Org. Lett.* **2016**, *18*, 916–919. [[CrossRef](#)] [[PubMed](#)]
36. Grant, J.A.; Lu, Z.; Tucker, D.E.; Hockin, B.M.; Yufit, D.S.; Fox, M.A.; Katakya, R.; Chechik, V.; O'Donoghue, A.M.C. New Blatter-type radicals from a bench-stable carbene. *Nat. Commun.* **2017**, *8*, 15088. [[CrossRef](#)]
37. Constantinides, C.P.; Koutentis, P.A.; Rawson, J.M. Antiferromagnetic Interactions in 1D Heisenberg Linear Chains of 7-(4-Fluorophenyl) and 7-Phenyl-Substituted 1,3-Diphenyl-1,4-dihydro-1,2,4-benzotriazin-4-yl Radicals. *Chem. Eur. J.* **2012**, *18*, 15433–15438. [[CrossRef](#)]
38. Constantinides, C.P.; Koutentis, P.A.; Krassos, H.; Rawson, J.M.; Tasiopoulos, A.J. Characterization and Magnetic Properties of a “Super Stable” Radical 1,3-Diphenyl-7-trifluoromethyl-1,4-dihydro-1,2,4-benzotriazin-4-yl. *J. Org. Chem.* **2011**, *76*, 2798–2806. [[CrossRef](#)]
39. Bodzioch, A.; Zheng, M.; Kaszyński, P.; Utecht, G. Functional Group Transformations in Derivatives of 1,4-Dihydrobenzo [1,2,4]triazinyl Radical. *J. Org. Chem.* **2014**, *79*, 7294–7310. [[CrossRef](#)]
40. Tretyakov, E.; Fedyushin, P.; Bakuleva, N.; Korlyukov, A.; Dorovatovskii, P.; Gritsan, N.; Dmitriev, A.; Akyeva, A.; Syroeshkin, M.; Stass, D.; et al. Series of Fluorinated Benzimidazole-Substituted Nitronyl Nitroxides: Synthesis, Structure, Acidity, Redox Properties, and Magnetostructural Correlations. *J. Org. Chem.* **2023**, *88*, 10355–10370. [[CrossRef](#)]
41. Fedyushin, P.A.; Serykh, A.A.; Vinogradov, A.S.; Mezhenkova, T.V.; Platonov, V.E.; Nasyrova, D.I.; Samigullina, A.I.; Fedin, M.V.; Zayakin, I.A.; Tretyakov, E.V. Biradical with a polyfluorinated terphenylene backbone. *Russ. Chem. Bull.* **2022**, *71*, 1670–1678. [[CrossRef](#)]
42. Serykh, A.; Tretyakov, E.; Fedyushin, P.; Ugrak, B.; Dutova, T.; Lalov, A.; Korlyukov, A.; Akyeva, A.; Syroeshkin, M.; Bogomyakov, A.; et al. *N*-Fluoroalkylpyrazolyl-substituted Nitronyl Nitroxides. *J. Mol. Struct.* **2022**, *1269*, 133739. [[CrossRef](#)]
43. Fedyushin, P.A.; Akyeva, A.Y.; Syroeshkin, M.A.; Rybalova, T.V.; Stass, D.V.; Korolev, V.A.; Tretyakov, E.V.; Egorov, M.P. Synthesis, structure, and properties of *tert*-butyl perfluorobiphenyl nitroxide. *Russ. Chem. Bull.* **2022**, *71*, 1474–1482. [[CrossRef](#)]
44. Tretyakov, E.V.; Fedyushin, P.A. Polyfluorinated organic paramagnets. *Russ. Chem. Bull.* **2021**, *70*, 2298–2314. [[CrossRef](#)]
45. Politanskaya, L.V.; Fedyushin, P.A.; Rybalova, T.V.; Bogomyakov, A.S.; Asanbaeva, N.B.; Tretyakov, E.V. Fluorinated Organic Paramagnetic Building Blocks for Cross-Coupling Reactions. *Molecules* **2020**, *25*, 5427. [[CrossRef](#)] [[PubMed](#)]
46. Gurskaya, L.; Rybalova, T.; Beregovaya, I.; Zaytseva, E.; Kazantsev, M.; Tretyakov, E. Aromatic nucleophilic substitution: A case study of the interaction of a lithiated nitronyl nitroxide with polyfluorinated quinoline-*N*-oxides. *J. Fluor. Chem.* **2020**, *237*, 109613. [[CrossRef](#)]
47. Fedyushin, P.; Rybalova, T.; Asanbaeva, N.; Bagryanskaya, E.; Dmitriev, A.; Gritsan, N.; Kazantsev, M.; Tretyakov, E. Synthesis of Nitroxide Diradical Using a New Approach. *Molecules* **2020**, *25*, 2701. [[CrossRef](#)]
48. Tretyakov, E.; Fedyushin, P.; Pantaleeva, E.; Gurskaya, L.; Rybalova, T.; Bogomyakov, A.; Zaytseva, E.; Kazantsev, M.; Shundrina, I.; Ovcharenko, V. Aromatic S_N^F-Approach to Fluorinated Phenyl *tert*-Butyl Nitroxides. *Molecules* **2019**, *24*, 4493. [[CrossRef](#)] [[PubMed](#)]

49. Fedyushin, P.; Gurskaya, L.; Panteleeva, E.; Koshcheev, B.; Maksimov, A.; Rybalova, T.V.; Zaytseva, E.; Tretyakov, E. Exploration of S_N^F -Approach toward Functionalized Nitronyl Nitroxides. *Fluor. Notes* **2019**, *123*, 7–8.
50. Zhivetyeva, S.I.; Zayakin, I.A.; Bagryanskaya, I.Y.; Zaytseva, E.V.; Bagryanskaya, E.G.; Tretyakov, E.V. Interaction of a lithiated nitronyl nitroxide with polyfluorinated 1,4-naphthoquinones. *Tetrahedron* **2018**, *74*, 3924–3930. [[CrossRef](#)]
51. Fedyushin, P.; Panteleeva, E.; Bagryanskaya, I.; Maryunina, K.; Inoue, K.; Stass, D.; Tretyakov, E. An approach to fluorinated phthalonitriles containing a nitronyl nitroxide or iminonitroxide moiety. *J. Fluor. Chem.* **2019**, *217*, 1–7. [[CrossRef](#)]
52. Tretyakov, E.V.; Fedyushin, P.A.; Panteleeva, E.V.; Stass, D.V.; Bagryanskaya, I.Y.; Beregovaya, I.V.; Bogomyakov, A.S. Substitution of a Fluorine Atom in Perfluorobenzonitrile by a Lithiated Nitronyl Nitroxide. *J. Org. Chem.* **2017**, *82*, 4179–4185. [[CrossRef](#)] [[PubMed](#)]
53. Potts, K.T.; Roy, S.K.; Jones, D.P. 1,2,4-Triazoles. XVII. Meso-ionic compounds. 2. Derivatives of the s-triazole series. *J. Org. Chem.* **1967**, *32*, 2245–2252. [[CrossRef](#)]
54. Steen, J.S.; Nuismier, J.L.; Eiva, V.; Wiglema, A.E.T.; Daub, N.; Hjelm, J.; Otten, E. Blatter Radicals as Bipolar Materials for Symmetrical Redox-Flow Batteries. *J. Am. Chem. Soc.* **2022**, *144*, 5051–5058. [[CrossRef](#)]
55. Constantinides, C.P.; Berezin, A.A.; Manoli, M.; Leitus, G.M.; Bendikov, M.; Rawson, J.M.; Koutentis, P.A. Effective exchange coupling in alternating-chains of a π -extended 1,2,4-benzotriazin-4-yl. *New J. Chem.* **2014**, *38*, 949–954. [[CrossRef](#)]
56. Constantinides, C.P.; Berezin, A.A.; Manoli, M.; Leitus, G.M.; Zissimou, G.Z.; Bendikov, M.; Rawson, J.M.; Koutentis, P.A. Structural, Magnetic, and Computational Correlations of Some Imidazolo-Fused 1,2,4-Benzotriazinyl Radicals. *Chem. Eur. J.* **2014**, *20*, 5388–5396. [[CrossRef](#)]
57. Saal, A.; Friebe, C.; Schubert, U.S. Blatter radical as a polymeric active material in organic batteries. *J. Power Sources* **2022**, *524*, 231061. [[CrossRef](#)]
58. Bard, A.J.; Faulkner, L.R. *Electrochemical Methods: Fundamentals and Applications*, 2nd ed.; Wiley: New York, NY, USA, 2001.
59. Koutentis, P.A.; Re, D.L. Catalytic Oxidation of N-Phenylamidrazones to 1,3-Diphenyl-1,4-dihydro-1,2,4-benzotriazin-4-yls: An Improved Synthesis of Blatter's Radical. *Synthesis* **2010**, 2075–2079. [[CrossRef](#)]
60. Tretyakov, E.V.; Ovcharenko, V.I.; Terent'ev, A.O.; Krylov, I.B.; Magdesieva, T.V.; Mazhukin, D.G.; Gritsan, N.P. Conjugated nitroxides. *Russ. Chem. Rev.* **2022**, *91*, RCR5025. [[CrossRef](#)]
61. Tretyakov, E.V.; Petunin, P.V.; Zhivetyeva, S.I.; Gorbunov, D.E.; Gritsan, N.P.; Fedin, M.V.; Stass, D.V.; Samoilova, R.I.; Bagryanskaya, I.Y.; Shundrina, I.K.; et al. Platform for High-Spin Molecules: A Verdazyl-Nitronyl Nitroxide Triradical with Quartet Ground State. *J. Am. Chem. Soc.* **2021**, *143*, 8164–8176. [[CrossRef](#)]
62. Gubaidullin, A.T.; Buzykin, B.I.; Litvinov, I.A.; Gazetdinova, N.G. Molecular and Crystal Structure of a Superstable Free Radical, 1,3-Diphenyl-1,4-dihydro-1,2,4-benzotriazin-4-yl. *Russ. J. Gen. Chem.* **2004**, *74*, 939–943. [[CrossRef](#)]
63. You, X.; Xie, X.; Sun, R.; Chen, H.; Li, S.; Liu, Y. Titanium-mediated cross-coupling reactions of 1,3-butadiynes with α -iminonitriles to 3-aminopyrroles: Observation of an imino aza-Nazarov cyclization. *Org. Chem. Front.* **2014**, *1*, 940–946. [[CrossRef](#)]
64. Zhao, Y.; Gao, L.; Li, H.; Sun, P.; Meng, F.; Zhang, Y.; Xie, Y.; Sun, B.; Zhou, S.; Ma, Y.; et al. Synthesis, Insecticidal Activities, and Structure–Activity Relationship of Phenylpyrazole Derivatives Containing a Fluoro-Substituted Benzene Moiety. *J. Agric. Food Chem.* **2020**, *68*, 11282–11289. [[CrossRef](#)] [[PubMed](#)]
65. Duling, D.R. Simulation of multiple isotropic spin trap EPR spectra. *J. Magn. Reson. B* **1994**, *104*, 105–110. [[CrossRef](#)] [[PubMed](#)]
66. Bruker APEX3, RLATT, CELL_NOW, TWINABS, SAINT-Plus and SADABS; Bruker AXS Inc.: Madison, WI, USA, 2016.
67. Krause, L.; Herbst-Irmer, R.; Sheldrick, G.M.; Stalke, D. Comparison of silver and molybdenum microfocus X-ray sources for single-crystal structure determination. *J. Appl. Crystallogr.* **2015**, *48*, 3–10. [[CrossRef](#)]
68. Sheldrick, G.M. SHELXT—Integrated space-group and crystal-structure determination. *Acta Cryst. A* **2015**, *71*, 3–8. [[CrossRef](#)]
69. Sheldrick, G.M. Crystal Structure Refinement with SHELXL. *Acta Cryst. C* **2015**, *71*, 3–8. [[CrossRef](#)]
70. Nagao, H.; Nishino, M.; Shigetani, Y.; Soda, T.; Kitagawa, Y.; Onishi, T.; Yoshika, Y.; Yamaguchi, K. Theoretical studies on effective spin interactions, spin alignments and macroscopic spin tunneling in polynuclear manganese and related complexes and their mesoscopic clusters. *Coord. Chem. Rev.* **2000**, *198*, 265–295. [[CrossRef](#)]
71. Soda, T.; Kitagawa, Y.; Onishi, T.; Nagao, H.; Yoshioka, Y.; Yamaguchi, K. Ab initio computations of effective exchange integrals for H–H, H–He–H and Mn2O2 complex: Comparison of broken-symmetry approaches. *Chem. Phys. Lett.* **2000**, *319*, 223–230. [[CrossRef](#)]
72. Lee, C.; Yang, W.; Parr, R.G. Development of the Colle-Salvetti correlation-energy formula into a functional of the electron density. *Phys. Rev. B* **1988**, *37*, 785–789. [[CrossRef](#)]
73. Becke, A.D. Density-functional thermochemistry. III. The role of exact exchange. *J. Chem. Phys.* **1993**, *98*, 5648–5652. [[CrossRef](#)]
74. Weigend, F.; Ahlrichs, R. Balanced basis sets of split valence, triple zeta valence and quadruple zeta valence quality for H to Rn: Design and assessment of accuracy. *Phys. Chem. Chem. Phys.* **2005**, *7*, 3297–3305. [[CrossRef](#)]
75. Grimme, S.; Antony, J.; Ehrlich, S.; Krieg, H. A consistent and accurate ab initio parametrization of density functional dispersion correction (DFT-D) for the 94 elements H–Pu. *J. Chem. Phys.* **2010**, *132*, 154104. [[CrossRef](#)] [[PubMed](#)]
76. Grimme, S. Semiempirical GGA-type density functional constructed with a long-range dispersion correction. *J. Comput. Chem.* **2006**, *27*, 1787–1799. [[CrossRef](#)] [[PubMed](#)]
77. Weigend, F. Accurate Coulomb-fitting basis sets for H to Rn. *Phys. Chem. Chem. Phys.* **2006**, *8*, 1057–1065. [[CrossRef](#)]
78. Barone, V.; Cossi, M. Quantum Calculation of Molecular Energies and Energy Gradients in Solution by a Conductor Solvent Model. *J. Phys. Chem. A* **1998**, *102*, 1995–2001. [[CrossRef](#)]

79. Adamo, C.; Barone, V. Toward Reliable Density Functional Methods without Adjustable Parameters: The PBE0 Model. *J. Chem. Phys.* **1999**, *110*, 6158–6170. [[CrossRef](#)]
80. Dreuw, A.; Head-Gordon, M. Single-Reference ab Initio Methods for the Calculation of Excited States of Large Molecules. *Chem. Rev.* **2005**, *105*, 4009–4037. [[CrossRef](#)]
81. Neese, F. Software update: The ORCA program system—Version 5.0. *WIREs Comput. Mol. Sci.* **2022**, *12*, e1606. [[CrossRef](#)]
82. Kadilenko, E.M.; Gritsan, N.P.; Tretyakov, E.V.; Fokin, S.V.; Romanenko, G.V.; Bogomyakov, A.S.; Gorbunov, D.E.; Schollmeyer, D.; Baumgarten, M.; Ovcharenko, V.I. A black-box approach to the construction of metal-radical multispin systems and analysis of their magnetic properties. *Dalton Trans.* **2020**, *49*, 16916–16927. [[CrossRef](#)]

Disclaimer/Publisher's Note: The statements, opinions and data contained in all publications are solely those of the individual author(s) and contributor(s) and not of MDPI and/or the editor(s). MDPI and/or the editor(s) disclaim responsibility for any injury to people or property resulting from any ideas, methods, instructions or products referred to in the content.